Reduction Method for Real-Time Simulations in Hybrid Testing

Andersen, Sebastian; Poulsen, Peter Noe

Published in:
Proceedings of EURODYN 2014

Publication date:
2014

Document Version
Peer reviewed version

Reduction Method for Real-Time Simulations in Hybrid Testing

Sebastian Andersen[1], Peter Noe Poulsen[2]
[1]Department of Civil Eng., Technical University of Denmark, PhD. Student, 2800 Kgs. Lyngby, Denmark
[2] Department of Civil Eng., Technical University of Denmark, Associate Professor, 2800 Kgs. Lyngby, Denmark
email: seba@byg.dtu.dk, pnp@byg.dtu.dk

ABSTRACT: Real-time hybrid testing combines testing of physical components with numerical simulations. The concept of the method requires that the numerical simulations should be executed in real time. However, for large numerical models including nonlinear behavior a combination of computationally costly assembling of the internal forces element by element at each equilibrium point and a strict requirement for small time steps to maintain accuracy and stability often prevents real time execution. Thus, enhanced numerical capacity is required. In the present study a basis reduction method is used to reformulate kinematic nonlinear equations of motion into a sum of constant matrices each multiplied by a reduced coordinate decreasing the assembling time. Furthermore the method allows for cutting off some of the higher frequency content not representing real physics decreasing the stability requirement for the time step. However, it is important that the chosen basis can represent the nonlinearities of the system. If not locking of the system can be a consequence ruining the accuracy of the results. To demonstrate the potential of the method in a real time simulation perspective and the importance of choosing a sufficient basis a composite beam and a cantilever beam including kinematic nonlinearities and exposed to harmonic loadings are analyzed. To reduce locking modes with higher order terms are included. From the analysis it is concluded that the method exhibits encouraging potential with respect to real time execution if a sufficient basis is chosen.

KEY WORDS: Kinematic Nonlinearities, Basis reduction, Real-time simulation, Finite Element Analysis.

1 INTRODUCTION

Hybrid testing is a testing method that was developed by Japanese scientists in the 1960's, cf. [1]. If conducted in real-time in order to include dynamic effects the method is often referred to as real-time hybrid testing (RTHT).

The principle of the method is that the considered structure is partitioned into two parts; a physical substructure and an analytical substructure. The physical component is a structural part that displays complicated or unknown structural behavior and therefore has to be tested in a physical test setup. The analytical substructure on the other hand is well understood. Thus, this part does not have to be tested but can instead be modeled numerically and solved by a time integration scheme. As only the component displaying complicated behavior has to be build and tested physically a full scale test can be conducted in more modest physical frames which makes it highly economically profitable.

During the hybrid test an iterative loop is running where the response of the numerical model found from the time integration is imposed onto the physical substructure through servo-hydraulic actuators in a finite number of points. The force response from the physical component is then measured by the actuators and sent to the numerical model. Together the experimental substructure(s), the analytical substructure(s), the integration algorithm and the servo-hydraulic actuators are integrated through an IT control system to form the real-time hybrid simulation system. For further details about the principle of Hybrid testing see e.g. [2-3].

For RTHT to be successful it is required that servo-hydraulic actuators are able to impose the displacements accurately onto the physical substructure in real time, that the communication between the analytical and physical substructure has a minimum delay and that the time integration is robust, accurate and fast to ensure real time execution.

The requirement that the numerical time integration has to be executed in real time limits the size of the nonlinear numerical substructures that can be applied in RTHT. Main part of the computation time in nonlinear analysis is due to the internal nodal forces computed element by element followed by an assembling into the global set of equations before each time step. When increasing the size of the numerical models the assembling time is obviously increased as well. Simultaneously, when increasing the size and complexity of the models higher frequencies are introduced, which calls for smaller time steps in the integration schemes in order to maintain stability and accuracy. Decreasing the time steps increases the computational time further as the number of assemblings of the internal nodal forces within a given simulated time interval are increased. Thus, increasing the size and complexity of the numerical substructures increases the computational time, which work against the real time execution requirement.

Both implicit and explicit algorithms and combinations of these are considered among researchers in RTHT context, see e.g. [4-10]. In [10] a selection of implicit and explicit integration schemes is evaluated in a RTHT setup with nonlinear substructures. The study concludes that explicit schemes are preferable. These schemes are simpler and do not require equilibrium iterations, making them less time consuming than implicit algorithms. However, the downside of explicit schemes is that smaller time steps are required to maintain stability of the system compared to implicit schemes.

The study in [10] also concludes that due to the performance of the time integration schemes the capacity with respect to degrees of freedom (dof) in the discretized system is very modest if real time execution should be performed. Under the given circumstances around 50 dofs in a nonlinear context dictates the upper limit. As far as known the maximum number of dof's used in a RTHT with a nonlinear analytical substructure is 134, cf. [11]. Thus, a very interesting

and important issue related to RTHT is how to improve the computational capacity in order to be able to simulate the response of large and complex numerical substructures including nonlinear effects in real time.

One way of decreasing the computational time is by using reduced order modeling (ROM) reducing the discretized nonlinear equations of motion by projecting them onto a subspace represented by a reduced basis. This is a simple way to reduce the number of dof's and at the same time to cut off some of the higher frequency content contained in the model not representing real physics. The latter allows one to increase the time steps whereby the assembling frequency of the internal nodal forces and thereby the computation time are reduced.

In [12] the concept of ROM is described together with an overview and evaluation of the most common used bases for kinematic nonlinear structures considering robustness and accuracy. From the study it is concluded that linear normal modes are among the best performing bases under the given circumstances despite the fact that they neglects the nonlinear nature of the system.

In [13] is considered a material nonlinear structure. To model the response a reduced basis consisting of a number of Ritz vectors encapsulating the material nonlinear response is used. The Ritz-basis is derived from a combination of linear normal modes and a number of plastic deformation shapes found from a static analysis. The basis is introduced into a set of linear equation of motion whereby the costly assembling every time step is avoided. This enables the authors to model the response of a 50-dof nonlinear plastic model with three elastic and six plastic modes in real time. However, the plastic modes obtained in this way possessed high frequencies which had to be decreased artificially by including additional inertia to be able to perform real-time simulations. Furthermore, the approach is not very suitable for systems with alternately increase and decrease in stiffness which is the case for kinematic nonlinear structures.

When using ROM for nonlinear systems the time consuming assembling of the nonlinear internal nodal forces is still required in every time step before projecting them onto the reduced subspace. As an answer to this problem researchers in [14] have presented a reduced basis formulation (RBF) where the discretized equations of motion by a simple mathematical reformulation can be written as a sum of stiffness matrix terms that remain constant throughout the entire analyses each multiplied by a reduced coordinate in the projected subspace. For a subspace consisting of m modes $1+m+m^2$ constant matrix terms are arranged. This reformulation enables a much faster assembling of the nonlinear internal nodal forces compared to the usual assembling element by element.

To the best of the present authors' knowledge no study has been performed illustrating the potential of the method in [14] in a real-time perspective. Thus, in the present study the RBF is used to analyze kinematic nonlinear structures in a real-time perspective to illustrate the applicability in nonlinear real time analysis. Two examples are considered. The first example constitutes a composite beam exposed to harmonic loadings. The beam parameters are based on inspiration from a composite beam planned to be tested in a RTHT arrangement at the Technical University of Denmark (DTU) in the spring 2014, making the example relevant in that perspective.

As will be evident to the reader the analysis of the composite beam is exposed to the phenomena of locking ruining the results. The locking effect is introduced through the choice of basis consisting of purely linear modes. To reduce the effect of this, modes containing higher order terms can be included. This is illustrated in a second example considering a simple cantilever beam.

In section 2 the RBF by [14] is presented together with a reduction of the formulation taking symmetry conditions into account. In section 3 an approach to include higher order terms to the linear normal modes are presented. Finally in section 4 and 5 the examples of the composite and cantilever beams, respectively, are described, analysed and discussed. In section 6 the conclusion is given.

2 REDUCED BASIS FORMULATION

In the following section the RBF developed by [14] is used to reduce a set of discretized kinematic nonlinear equations of motion. Furthermore an improvement of the formulation taking into account symmetry conditions is presented.

2.1 Nonlinear modal equations

The starting point of the method is the global set of discretized nonlinear equations of motion in physical coordinates containing n dofs written in matrix notation

$$\mathbf{M}\ddot{\mathbf{V}} + \mathbf{C}\dot{\mathbf{V}} + \mathbf{g}(\mathbf{V}) = \mathbf{F}(t) \tag{1}$$

where **M** and **C** are *n x n* mass and damping matrices, **F**(t) a *n x 1* external load vector which is a function of time and **g**(**V**) a *n x 1* vector containing internal restoring forces. Finally **V** is a *n x 1* vector representing the nodal displacement in global format where a dot above the vector denotes a time derivative. In the given case the discretized system in (1) is based on continuum mechanics with Green strain characterizing the state of deformation and with the Second Piola-Kirchoff stresses as conjugate stress components, cf. Appendix 1.

In the present only the internal restoring forces, **g**(**V**), are assumed to be a nonlinear function of the nodal displacements. The nonlinear restoring forces consist of a constant, linear and a quadratic stiffness matrix contribution in **V**

$$\mathbf{g}(\mathbf{V}) = (\mathbf{K}^0 + \mathbf{K}^1(\mathbf{V}) + \mathbf{K}^2(\mathbf{V},\mathbf{V}))\mathbf{V} \tag{2}$$

where $\mathbf{K}^0$ is the constant stiffness matrix known from linear elastic theory and $\mathbf{K}^1$ and $\mathbf{K}^2$ are linear and quadratic functions of the **V**, respectively, introduced due to the kinematic nonlinearities.

The discretized nonlinear equation of motion in physical coordinates can be projected onto a reduced subspace by introducing a relation between the physical and reduced coordinates given as

$$\mathbf{V} = \mathbf{\Phi}\mathbf{S} = \sum_{i=1}^{m} \boldsymbol{\varphi}_i S_i \tag{3}$$

where **Φ** is a *m x m* matrix containing m basis', $\boldsymbol{\varphi}_i$, arranged as columns and **S** a *m x 1* vector containing the m reduced

coordinates, s_i. The number of reduced basis are usually much smaller than the number of dofs, i.e. $m << n$.

Projecting the discretized equations in (1) onto the reduced subspace represented by (3) yields the general formulation

$$\tilde{\mathbf{M}}\ddot{\mathbf{S}} + \tilde{\mathbf{C}}\dot{\mathbf{S}} + \tilde{\mathbf{g}}(\mathbf{S}) = \tilde{\mathbf{F}}(t) \tag{4}$$

with the introduced vectors and matrices

$$\begin{aligned} \tilde{\mathbf{M}} &= \mathbf{\Phi}^T \mathbf{M} \mathbf{\Phi} \\ \tilde{\mathbf{C}} &= \mathbf{\Phi}^T \mathbf{C} \mathbf{\Phi} \\ \tilde{\mathbf{g}}(\mathbf{S}) &= \mathbf{\Phi}^T \mathbf{g}(\mathbf{\Phi S}) \end{aligned} \tag{5}$$

In [14] the nodal restoring forces in (5) are written as a sum using the right hand side of (3). This leads to the general formulation for the reduced internal nodal forces

$$\tilde{\mathbf{g}}(\mathbf{S}) = (\tilde{\mathbf{K}}^0 + \sum_{i=1}^{m} \tilde{\mathbf{K}}_i^1 s_i + \sum_{i=1}^{m}\sum_{j=1}^{m} \tilde{\mathbf{K}}_{ij}^2 s_i s_j)\mathbf{S} \tag{6}$$

where all matrices appearing in (6) are constants. In Appendix 2 the formulation of the matrices based on Continuum mechanics are presented.

As the matrices appearing in (6) are constants these can be built before initiating the time integration if keeping the same basis throughout the analysis. This allows for a fast assembling of the nodal forces in (6) between each time step compared to the usual costly assembling of the internal nodal forces performed element by element.

2.2 Symmetry reduction of quadratic sum

The formulation of the restoring forces in (6) can compacted even further by taking advantage of the symmetry of the products of the reduced coordinates

$$s_i s_j = s_j s_i \tag{7}$$

By introducing the definition

$$\tilde{\mathbf{K}}_{ij}^{2*} = \tilde{\mathbf{K}}_{ij}^2 + (1-\delta_{ij})\tilde{\mathbf{K}}_{ji}^2 \tag{8}$$

The symmetry condition in (7) allows the quadratic sum in (6) to be written as

$$\sum_{i=1}^{m}\sum_{j=1}^{m} \tilde{\mathbf{K}}_{ij}^2 s_i s_j = \sum_{i=1}^{m}\left(\sum_{j=1}^{i} \tilde{\mathbf{K}}_{ij}^{2*} s_i s_j \right) \tag{9}$$

This reduces the number of sums by the number

$$m_{reduced} = m^2 - \frac{m^2 - m}{2} = \frac{m^2 - m}{2} \tag{10}$$

corresponding to a relative reduction of magnitude

$$r = \frac{m_{reduced}}{m^2} = \frac{(\mathrm{m}-1)}{2m} \tag{11}$$

In the limit state this approaches a reduction of magnitude

$$\lim_{m\to\infty} r = \frac{1}{2} = 50\% \tag{12}$$

3 MODES INCLUDING HIGHER ORDER EFFECTS

Choosing a reduction basis consisting of linear modes from the undeformed stage might causes the nonlinear coupling effects of the structure to be locked as these effects are not accounted for by the linear normal modes. This will increase the stiffness of the system and thereby affect the accuracy of the results. To prevent these locking phenomena modes containing higher order terms can be included.

Considering a linear normal mode i, $\mathbf{\Phi}_i$, an estimate for a mode, $\mathbf{\Phi}_i^h$, representing the higher order terms of the linear mode can be found by performing a nonlinear static calculation considering an equivalent formulation of the eigenvalue problem (EVP). Considering the mass times the considered linear mode as an external load and replacing the square of the natural frequency by a scaling factor α a nonlinear static system of equations can be arranged as

$$\mathbf{K}(\mathbf{\Phi})\mathbf{\Phi} = \alpha \mathbf{M} \mathbf{\Phi}_i \tag{13}$$

By scaling the load factor α such that the solution vector $\mathbf{\Phi}$ deviates slightly from the linear solution a vector estimate for the higher order terms of $\mathbf{\Phi}_i$, can be taken as the difference between the linear normal mode and the static solution

$$\mathbf{\Phi}_i^h = \mathbf{\Phi} - \mathbf{\Phi}_i \tag{14}$$

These modes will be applied in the analysis of the cantilever beam in section 5. The modes $\mathbf{\Phi}_i^h$ used in this example case are based on solutions where the maximum deviation in a discretization point between the linear and nonlinear response, $\mathbf{\Phi}$ and $\mathbf{\Phi}_i$, was around 1%.

4 ANALYSIS OF COMPOSITE BEAM

In the following section a composite beam is analysed to illustrate the potential of the RBF described in section 2 in a real-time perspective. Furthermore the example illustrates the consequence of locking introduced if the chosen basis cannot represent the nonlinear coupling effects.

First is presented the description of the composite geometry, boundary conditions, general stiffness parameters and loading. Next the numerical modeling of the beam and the analysis approach is described. In the final section the analysis results are presented and discussed.

4.1 Geometry and boundary conditions of composite beam

In Figure 1 is sketched the composite beam in the x-z plane. The beam is of length L and simply supported at the beam ends with the rotation axis arranged in the bottom of the composite. The distance L_c marks a part of the beam where a section cut is made to increase the effect of the kinematic nonlinearities.

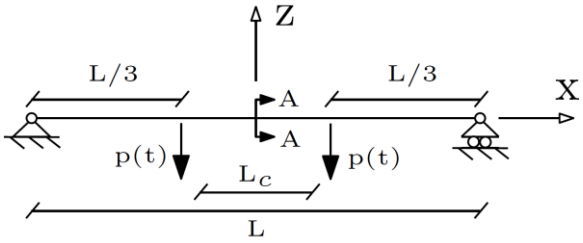

Figure 1. Composite beam in x-z plane.

In Figure 2 the cross section through section A-A marked in Figure 1 is sketched. From the figure the composite is seen to be hollow with an exterior height B and a width H. The wall thicknesses are t_1 and t_2 along the height and width respectively and the curvature along the edges of the profile is r. The introduced section cut is of width h and is placed in the flange in a distance t_2+r from the outer edge of the web. Finally point A marks an edge point at the section cut which will be considered in the analysis.

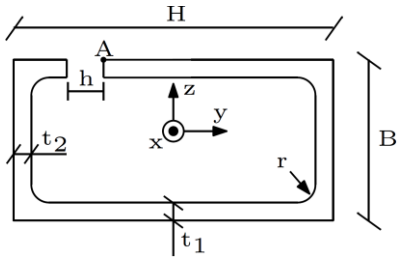

Figure 2. Composite cross section at section A-A.

In Table 1 are listed the geometry parameters of the composite beam.

Table 1. Geometry parameters of composite beam

Parameter	Magnitude	Unit
L	5	m
L_c	1	m
H	0.132	m
B	0.054	m
R	0.006	m
t_1, t_2	0.002	m
H	0.004	m
A	680	mm^2

4.2 Loading of composite beam

The beam is loaded by a periodic loading

$$p(t) = F_1 \sin(\omega_1 t) + F_2 \sin(\omega_2 t) \qquad (15)$$

with F_1 and F_2 denoting the load amplitudes and ω_1 and ω_2 the load frequencies

Table 2. Loading parameters for composite beam

Parameter	Magnitude	Unit
F_1	2	kN
F_2	1.25	kN
ω_1	5.20	Hz
ω_2	58.20	Hz

As illustrated in Figure 1 the resultant loads are applied a distance L/3 from the beam edges. They are distributed over a square area of size $(0.4 \times H)^2$ at the bottom flange. The load parameters are presented in Table 2. The load frequencies span the frequency domain of the ten first modes of the composite in the undeformed stage.

4.3 Stiffness parameters

The composite beam consists of a synthetic matrix material reinforced with longitudinal fibers in one direction of the beam. In Table 3 are listed the stiffness's parameters used in the analysis with the subscript referring the global direction indicated in Figure 1 and Figure 2. The parameters are taken from [19].

Table 3. Stiffness and material parameters of composite

Parameter	Magnitude	Unit
E_x	23	GPa
E_y, E_z	8.5	GPa
G	3	GPa
ν_{xy}, ν_{xz}	0.230	-
ν_{yx}, ν_{zx}	0.085	-
ν_{yz}, ν_{zy}	0.230	-
ρ	1825	kg/m^3

E_x, E_y, E_z denote the orthotropic moduli of elasticity and G denote the orthotropic shear moduli for shear deformation assumed equal in all planes, respectively. The term ν_{xy} is a Poisson ratio characterizing the strain in the y-direction produced by the stress in the x-direction. Similar interpretations are given for the remaining Poison ratios listed in Table 3. Finally ρ denotes the density of the composite.

In the given case it is assumed that the fibers are aligned parallel with the length of the beam leading to maximum stiffness moduli in the x-direction

4.4 Numerical Modeling

The composite beam is modeled in a local MATLAB based finite element program named BYGFEM. To model the structure the 10-nodal isoparametric tetrahedral element sketched in Figure 3 is used. The element can describe displacement fields up to 2nd order and stress fields up to 1st order correctly. Three translations describe the deformation in each node. For a more thorough description of the element, see e.g. [15].

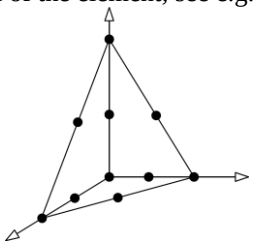

Figure 3. 10-nodal tetrahedral element.

To perform the time integration when using the RBF is used the *central difference method* (CDM) which is an explicit 2nd order method, see e.g. [15]. The reason for picking this integration scheme is that it is simple whereas the disadvantage is that the time step has to be below a critical value in order to prevent instability. To check the accuracy of the RBF solution this is compared to a full solution found with an implicit Newmark algorithm (NA).

In Table 4 are listed some of the algorithm parameters used in the analysis with t_{act} denoting the actual time simulated, Δt the time step magnitude with the superscript referring to the method applied and the algorithm parameters α and β applied in the full implicit analysis. The latter two are set equal to a magnitude corresponding to unconditionally stability in the linear analysis case. Finally ϵ is the equilibrium tolerance.

Table 4. Algorithm parameters

Parameter	Magnitude	Unit
t_{act}	0.25	s
Δt^{NA} / Δt^{CDM}	10^{-3} / $3 \cdot 10^{-5}$	s
ϵ	10^{-3}	-
γ	½	-
β	¼	-

Two different mesh sizes were used in the analysis. In the region spanning the section cut of length L_c (cf. Figure 1) the mesh density is set to ten times finer than in the remaining structure in order to model the curvature at the section cut sufficient. A total of 65523 dofs were contained in the model.

The basis used in the RBF is taken as the lowest 25 linear normal modes of the composite in the undeformed stage.

4.5 Analysis results and discussion

In Figure 4 is plotted the displacement, u_z, in point A (cf. Figure 2) in the time interval $t \in [0, 0.04]$ sec. The blue curve shows the solution obtained with the implicit NA representing the full solution. The red curve shows the RBF solution.

From the figure it is observed that the RBF curve starts to deviate significantly from the full model solution already from around t = 0.02 seconds. Around this point the RBF curve reaches a local maximum whereas the NA response keeps increasing rapidly. The behavior of the two curves indicate that the RBF solution exhibits a much higher stiffer than the NA solution. As indicated previously and as will be demonstrated in the example in the next section the increased stiffness is introduced through the choice of modes included in the model. Due to the kinematic nonlinearities coupling of the transverse and axial deformations take place. If the chosen modes do not represent these coupling effects sufficiently locking will appear increasing the stiffness of the system.

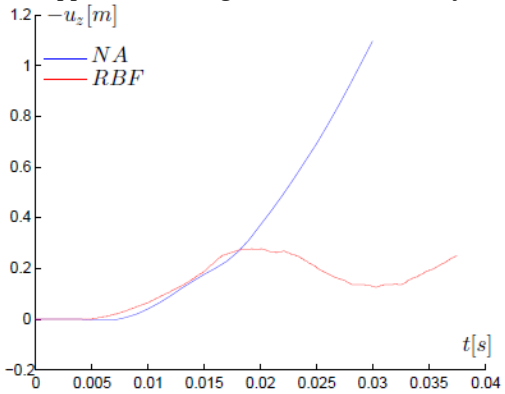

Figure 4. Displacement, u_z, at point A in the composite beam found using a NA and the RBF, respectively.

One way to overcome the locking phenomena is by increasing the number of modes until a sufficiently number of modes can represent these nonlinear effects. However, in order for the RBF to be performed in real time it is necessary to keep the number of modes as few as possible while still being able to describe the response as good as possible.

In Table 5 is presented how many modes that can be contained in the model for different time step magnitudes if the RBF should be executed in real time. It should be stressed that the results are based on simulations on a standard PC.

Table 5. Mode limit vs. time step magnitude

Time step [s]	No. of modes
10^{-3}	35
10^{-4}	12
10^{-5}	1

The table shows a decrease in number of modes as the time step is decreased, which should be expected. For a time step of magnitude $\Delta t = 10^{-5}$ a model approximated by one mode only can be executed in real time, whereas by increasing the time step to $\Delta t = 10^{-4}$ sec enables one to describe the response with up to 12 modes. Decreasing the time step further to $\Delta t = 10^{-3}$ sec up to 35 modes can be applied. As the time step is dictated by the highest frequency of the system through the stability requirement, the time step that can be applied is restricted by the nature of the considered system. Thus, the RBF is most suitable for low frequency ranges as this allows for larger time steps. From the table it is also evident that 25 modes are way beyond the limit for real time execution for the given time step applied analyzing the composite beam. However, the example in the next section indicates that by using only a few higher order modes the results can be improved significantly.

5 ANALYSIS OF CANTILEVER BEAM

A cantilever beam exposed to a harmonic loading is analysed next. The example serves to illustrate that the locking effect of a nonlinear response can be reduced significantly by introducing few modes including higher order effects.

5.1 Geometry, loading & stiffness parameters of cantilever

The cantilever is of length L and has a cross section of width and height w and h, cf. Figure 5.

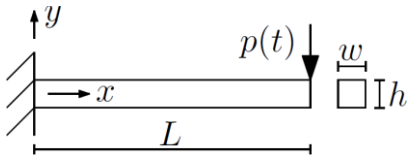

Figure 5. Sketch of cantilever exposed to sinusoidal load (left) and it cross section dimensions (right).

It is exposed to a sinusoidal load with amplitude F and excitation frequency ω.

$$p(t) = F \sin(\omega \cdot t) \tag{16}$$

The cantilever is isotropic and made from steel. The load amplitude F is chosen such that the response is significantly nonlinear. The frequency, ω, corresponds to 1/25 of the lowest natural frequency in the undeformed stage.

In Table 6 are presented the beam and load parameters.

Table 6. Cantilever parameters

Parameter	Magnitude	Unit
E	210	GPa
ν	0.3	GPa
h, w	1	m
L	4	m
F	2	GPa
ω	2	Hz

5.2 Numerical modeling

The cantilever is modeled with a mesh consisting of four elements along the height, twelve elements along the length and one element in the width direction with the tetrahedral element presented previously.

As for the composite beam the response of the cantilever beam is analysed numerically using the implicit NA and the CDM algorithm for the RBF with the algorithm parameters in Table 4.

In the present analysis the basis chosen for the RBF analysis consists of a varying number of modes. To reduce the locking effects linear modes and their corresponding higher order modes are included as determined by (13)-(14) using a Newton-Raphson algorithm. In Table 7 are listed three combinations of modes used.

Table 7. Modes included in RBF solutions

Case	Linear modes no.	Higher order modes no.
RBF 1	1-4	-
RBF 2	1	1
RBF 3	1, 4	1, 4

In the ‘RBF 1’-case the linear modes 1 to 4 are included without higher order terms. These modes constitute bending modes in the load direction (mode 1 and 4) whereas mode 2 and 3 constitute a bending mode opposite to the load direction and a torsional load around the beam axis. In the ‘RBF 2’- and ‘RBF 3’-case only the bending modes in the load plane together with their higher order modes are considered.

5.3 Analysis of Cantilever

In Figure 6 is plotted the response of the cross-sectional midpoint node at the loaded beam end. The blue curve represents NA solution whereas the remaining curves represent the RBF solutions.

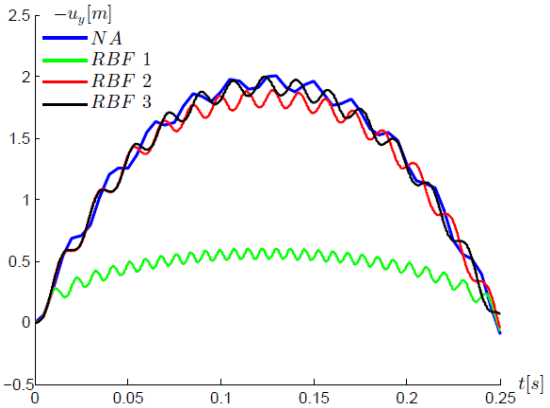

Figure 6. Deformation of midpoint node at loaded end.

Considering the full response the deformation it is seen to be dominated by a frequency equal to the excitation frequency with amplitude around 2 m corresponding to the static nonlinear response of the beam if exposed to the load amplitude, F. Local oscillations appear with a frequency around 50 Hz corresponding to the first linear bending mode of the beam. This mode is only slightly excited due to the relatively slower load frequency. The response in the ‘RBF 1’-case identifies a similar locking phenomenon indicated by the relatively small global amplitude and the increased local frequency response. By including the higher order modes the locking effects are seen to be significantly reduced as the curves ‘RBF 2’ and ‘RBF 3’ attain amplitudes close to the NA solution. The solutions ‘RBF 2’ and ‘RBF 3’ are not fully converged, but their results indicate that by adding few additional modes with higher order terms the response can improved significantly.

6 CONCLUSION

It has been demonstrated how to reduce a set of kinematic nonlinear equations of motion applying a reduced basis formulation (RBF) introduced by [14] making it possible to perform fast nodal force assembling. The formulation was improved using a symmetry condition reducing the number of assembling terms by fifty percent in the limit state. A composite beam exposed to a periodic loading was used as example to demonstrate the potential of the RBF. The results were influenced by locking introduced through the choice of included linear modes increasing the stiffness of the model. However, by adding a few higher order modes to the basis it was shown that the locking could be significantly reduced. This was illustrated in a simple example considering a cantilever beam. Furthermore it was concluded that time steps of magnitude 10^{-3} s, 10^{-4} s and 10^{-5} s allow the simulations to be performed in real time with up to around 35, 12 and 1 mode(s), respectively, on a standard PC. Based on this it is concluded that the RBF has potential to perform real time simulations if choosing a sufficient basis and if possible to go beyond a time step of 10^{-5} sec.

7 APPENDICES

In Appendix 1 the Continuum mechanics theory required for a finite element formulation is presented. In Appendix 2 the discretized equations of motion are derived based on the presented Continuum mechanics. Finally in Appendix 3 the definitions of the constant matrices in the sum-formulation in (6) are presented.

7.1 Appendix 1 – Generalized Strains and Stresses

In the present Continuum theory required to arrange the finite element formulations is presented. The Green Strain measure is chosen to characterize the state of deformation of the continuum considered with the conjugate stress given as the Second-Piola Kirchoff stress measure. A detailed description of the theory can be seen in e.g. [16-17].

The starting point is the general Green strain tensor

$$E_{ij} = \frac{1}{2}\left(\frac{\partial u_i}{\partial x_j^0} + \frac{\partial u_j}{\partial x_i^0}\right) + \frac{1}{2}\frac{\partial u_\gamma}{\partial x_j^0}\frac{\partial u_\gamma}{\partial x_i^0} = \frac{1}{2}\left(F_{ik}^T F_{kj} - \delta_{ij}\right) \tag{17}$$

and its variation

$$\delta E_{ij} = \frac{1}{2}\left(\frac{\partial x_\gamma}{\partial x_i^0}\frac{\partial(\delta u_\gamma)}{\partial x_j^0} + \frac{\partial(\delta u_\gamma)}{\partial x_i^0}\frac{\partial x_\gamma}{\partial x_j^0}\right) = \frac{1}{2}\left(F_{ik}^T \delta D_{kj} + \delta D_{ik}^T F_{kj}\right) \tag{18}$$

Where δ_{ij} is Kronecker's delta, F the deformation gradient, and D the displacement gradient given as

$$F_{ij} = \frac{\partial x_i}{\partial x_j^0} = \delta_{ij} + D_{ij} = [\mathbf{\delta}_1 + \mathbf{d}_1 \;\; \mathbf{\delta}_2 + \mathbf{d}_2 \;\; \mathbf{\delta}_3 + \mathbf{d}_3] \tag{19}$$

$$D_{ij} = \frac{\partial u_i}{\partial x_j^0} = [\mathbf{d}_1 \quad \mathbf{d}_2 \quad \mathbf{d}_3] \tag{20}$$

$$\delta D_{ij} = \frac{\partial(\delta u_i)}{\partial x_j^0} = [\delta\mathbf{d}_1 \quad \delta\mathbf{d}_2 \quad \delta\mathbf{d}_3] \tag{21}$$

As stated on the right hand side of (19)-(21) the tensors can be arranged as column vectors. This formulation is used to organize the finite element formulation in the following section.

The seond Piola-Kirchoff stress measure, S, is related to the Green strain tensor, E, through the constitutive relation assuming a *Saint Venant-Kirchoff material*

$$S_{ij} = C_{ijkl}E_{kl} \tag{22}$$

where C_{ijkl} is a fourth-order tensor of elastic moduli which are constant. It is often computationally convenient to represent the stress and strain components as a one-dimensional array. These are therefore organized in Voigt notation. For the given case considering orthotropic material this is given as, se e.g. [18]

$$C = \frac{1}{\nu_{12}\nu_{23}\nu_{31} + \nu_{13}\nu_{21}\nu_{32} + \nu_{12}\nu_{21} + \nu_{13}\nu_{31} + \nu_{23}\nu_{32} - 1} \times \begin{bmatrix} E_x(\nu_{yz}\nu_{zy} - 1) & -E_x(\nu_{yz}\nu_{zx} + \nu_{yx}) & -E_x(\nu_{yx}\nu_{zy} + \nu_{zx}) & 0 & 0 & 0 \\ & E_y(\nu_{xz}\nu_{zx} - 1) & -E_y(\nu_{xy}\nu_{zx} + \nu_{zy}) & 0 & 0 & 0 \\ & & E_z(\nu_{xy}\nu_{yx} - 1) & 0 & 0 & 0 \\ & & & G_{yz} & 0 & 0 \\ & sym & & & G_{xz} & 0 \\ & & & & & G_{xy} \end{bmatrix} \tag{23}$$

Introducing the definition in (19)-(20) into the green strain tensor in (17) this can be written in Voigt notation as

$$\mathbf{E} = [E_{11}\, E_{22}\, E_{33}\, 2E_{23}\, 2E_{13}\, 2E_{12}]^T = \begin{Bmatrix} \mathbf{\delta}_1^T\mathbf{d}_1 \\ \mathbf{\delta}_2^T\mathbf{d}_2 \\ \mathbf{\delta}_3^T\mathbf{d}_3 \\ \mathbf{\delta}_2^T\mathbf{d}_3 + \mathbf{\delta}_3^T\mathbf{d}_2 \\ \mathbf{\delta}_1^T\mathbf{d}_3 + \mathbf{\delta}_3^T\mathbf{d}_1 \\ \mathbf{\delta}_1^T\mathbf{d}_2 + \mathbf{\delta}_2^T\mathbf{d}_1 \end{Bmatrix} + \frac{1}{2}\begin{Bmatrix} \mathbf{d}_1^T\mathbf{d}_1 \\ \mathbf{d}_2^T\mathbf{d}_2 \\ \mathbf{d}_3^T\mathbf{d}_3 \\ 2\mathbf{d}_2^T\mathbf{d}_3 \\ 2\mathbf{d}_1^T\mathbf{d}_3 \\ 2\mathbf{d}_1^T\mathbf{d}_2 \end{Bmatrix} = \mathbf{E}_{lin} + \mathbf{E}_{nonlin} \tag{24}$$

7.2 Appendix 2 – Finite Element Formulation

In the present appendix the formulation of the element local discretized equations of motion are presented. The element local variation, **u**, is interpolated in terms of the end point nodal degrees of freedom contained in the vector **v** as

$$\mathbf{u} = \mathbf{N}\mathbf{v} \tag{25}$$

Where **N** is the displacement interpolation matrix **N** for an element with m degrees of freedom. With this the vectors $\mathbf{d}_j$ in (18) can be formulated as

$$\mathbf{d}_j = \frac{\partial u_i}{\partial x_j^0} = \frac{\partial}{\partial x_j^0}\mathbf{N}\mathbf{v} = \mathbf{B}_j\mathbf{v} \tag{26}$$

The corresponding virtual components to (27) is

$$\delta\mathbf{d}_j = \mathbf{B}_j\delta\mathbf{v} \tag{27}$$

Introducing the notations

$$2\mathbf{d}_i^T\mathbf{d}_j = \mathbf{d}_i^T\mathbf{d}_j + \mathbf{d}_j^T\mathbf{d}_i = \mathbf{v}^T\mathbf{B}_i^T\mathbf{B}_j\mathbf{v} + \mathbf{v}^T\mathbf{B}_j^T\mathbf{B}_i\mathbf{v} = \mathbf{v}^T(\mathbf{B}_i^T\mathbf{B}_j + \mathbf{B}_j^T\mathbf{B}_i)\mathbf{v} \tag{28}$$

$$\left(1 - \frac{1}{2}\delta_{ij}\right)\left(\mathbf{B}_i\mathbf{B}_j + \mathbf{B}_j\mathbf{B}_i\right) = \mathbf{B}_{ij} \tag{29}$$

The nonlinear vector $\mathbf{E}_{nonlin}$ in (24) can be written as

$$\mathbf{E}_{non} = \frac{1}{2}\left[\mathbf{v}^T\mathbf{B}_{11}\;\; \mathbf{v}^T\mathbf{B}_{22}\;\; \mathbf{v}^T\mathbf{B}_{33}\;\; \mathbf{v}^T\mathbf{B}_{23}\;\; \mathbf{v}^T\mathbf{B}_{13}\;\; \mathbf{v}^T\mathbf{B}_{12}\right]^T\mathbf{v} = \frac{1}{2}\mathbf{C}(\mathbf{v})\mathbf{v} \tag{30}$$

Where $\mathbf{C}(\mathbf{v})$ is a linear function of **v**. Furthermore by introducing the general expression for the linear strains known linear elastic theory

$$\mathbf{E}_{lin} = \mathbf{B}\mathbf{v} \tag{31}$$

With **B** denoting the strain interpolation matrix. The Green strain tensor in (24) can then be written in compact form as

$$\mathbf{E} = \mathbf{B}\mathbf{v} + \frac{1}{2}\mathbf{C}(\mathbf{v})\mathbf{v} \tag{32}$$

Due to symmetry of matrices in (33) the virtual Green strains on Voigt notation can be found as

$$\begin{aligned}\delta\mathbf{E} &= \mathbf{B}\delta\mathbf{v} + \frac{1}{2}\delta\mathbf{C}(\mathbf{v})\mathbf{v} + \frac{1}{2}\mathbf{C}(\mathbf{v})\delta\mathbf{v} \\ &= \mathbf{B}\delta\mathbf{v} + \mathbf{C}(\mathbf{v})\delta\mathbf{v}\end{aligned} \tag{33}$$

Now the internal nodal load vector **g**(**v**) can be organized from the virtual work equation in static context

$$\begin{aligned}\delta V_{\text{int}} &= \int_{V_0} \delta\mathbf{E}^T \mathbf{S}\, dV_0 \\ &= \int_{V_0} (\mathbf{B}\delta\mathbf{v} + \mathbf{C}\delta\mathbf{v})^T \mathbf{D}(\mathbf{B}\mathbf{v} + \frac{1}{2}\mathbf{C}\mathbf{v})\, dV_0 \\ &= \delta\mathbf{v}^T \mathbf{g}(\mathbf{v})\end{aligned} \tag{34}$$

With **D** denoting the material stiffness matrix. The matrix contribution in **g**(**v**) are constant terms, terms linear in **v** and terms quadratic in **v**, respectively. These are defined as

$$\begin{aligned}\mathbf{k}^0 &= \int_{V_0} \mathbf{B}^T\mathbf{D}\mathbf{B}\, dV_0 \\ \mathbf{k}^1(\mathbf{v}) &= \int_{V_0} \mathbf{C}(\mathbf{v})^T\mathbf{D}\mathbf{B} + \frac{1}{2}\mathbf{B}^T\mathbf{D}\mathbf{C}(\mathbf{v})\, dV_0 \\ \mathbf{k}^2(\mathbf{v},\mathbf{v}) &= \frac{1}{2}\int_{V_0} \mathbf{C}(\mathbf{v})^T\mathbf{D}\mathbf{C}(\mathbf{v})\end{aligned} \tag{35}$$

The nonlinear equations of motion are found by adding inertia and damping terms

$$\mathbf{m}\ddot{\mathbf{v}} + \mathbf{c}\dot{\mathbf{v}} + \mathbf{g}(\mathbf{v}) = \mathbf{f}(t) \tag{36}$$

With **m** being the mass matrix, **c** the damping matrix and **f**(t) the external load vector.

7.3 Appendix 3 – Formulation of modal matrices

In the following the expressions for the modal matrices in (6) based on the continuum theory presented in Appendix 1 are identified.

The local element dofs in **v** and the global dofs **V** are related through the element local topology array **L**

$$\mathbf{v} = \mathbf{L}\mathbf{V} = \mathbf{L}\boldsymbol{\varphi}_i s_i \tag{37}$$

Where the reduced basis formulation in (3) is introduced. Introducing this relation into the nonlinear part of the nodal forces in (33) and projecting this onto the reduced basis in (3) yields the expression

$$\begin{aligned}\boldsymbol{\Phi}^T\mathbf{g}^{non}(\mathbf{v}) = \boldsymbol{\Phi}^T\Big(\int_{V_0} \sum_{i=1}^{m} (\mathbf{C}^T(\mathbf{L}\boldsymbol{\varphi}_i)\mathbf{D}\mathbf{B} + \frac{1}{2}\mathbf{B}^T\mathbf{D}\mathbf{C}(\mathbf{L}\boldsymbol{\varphi}_i))\mathrm{s}_i + \\ \sum_{i=1}^{m}\sum_{j=1}^{m} \frac{1}{2}\mathbf{C}^T(\mathbf{L}\boldsymbol{\varphi}_i)\mathbf{D}\mathbf{C}(\mathbf{L}\boldsymbol{\varphi}_j)\mathrm{s}_i\mathrm{s}_j\Big)\boldsymbol{\Phi}\mathbf{s}\end{aligned} \tag{38}$$

From where the local element stiffness's in reduced coordinates are identified as

$$\begin{aligned}\tilde{\mathbf{k}}^1_{i,el} &= \boldsymbol{\Phi}^T\Big(\int_{V_0} \mathbf{C}^T(\mathbf{L}\boldsymbol{\varphi}_i)\mathbf{D}\mathbf{B} + \frac{1}{2}\mathbf{B}^T\mathbf{D}\mathbf{C}(\mathbf{L}\boldsymbol{\varphi}_i)\Big)\boldsymbol{\Phi}^T \\ \tilde{\mathbf{k}}^2_{ij,el} &= \boldsymbol{\Phi}^T\Big(\int_{V_0} \frac{1}{2}\mathbf{C}^T(\mathbf{L}\boldsymbol{\varphi}_i)\mathbf{D}\mathbf{C}(\mathbf{L}\boldsymbol{\varphi}_j)\Big)\boldsymbol{\Phi}\end{aligned} \tag{39}$$

The global stiffnesses in reduced coordinates presented in general form in (6) are found by summing over the total number of elements (nel)

$$\tilde{\mathbf{K}}^1_i = \sum_{el=1}^{nel} \tilde{\mathbf{k}}^1_{i,\text{el}}, \quad \tilde{\mathbf{K}}^2_{ij} = \sum_{el=1}^{nel} \tilde{\mathbf{k}}^2_{ij,el} \tag{40}$$

REFERENCES

[1] Hakuno, M. Shidawara, M. and Hara, T., *Dynamic destructive test of a cantilever beam, controlled by an analog-computer*, Transactions of the Japan Society of Civil Engineers, vol. 171, pp. 1-9, 1969 (in Japanese)

[2] C. Chen, J. M. Rickles, T. L. Karavasilis, Y. Chae, and R. Sause, *Evaluation of a real-time hybrid simulation system for performance evaluation of structures with rate dependent devices subjected to seismic loading*, Engineering Structures, Vol. 35, pp. 71-82, 2012.

[3] M. Verma and R. Rajasankar et al., *Improved Model for real-time sub-structuring testing system*, Engineering Structures, Vol. 41, pp. 258-269, 2012.

[4] R.-Y. Jung, P. B. Shing, E. Staufer and B. Thoen. *Performance of a real-time pseudodynamic test system considering nonlinear structural response*, Earthquake Engineering, Vol. 36, Issue 12, , pp. 1785-1809, 2007.

[5] D. Combescure & P. Pegon, *alpha-Operator Splitting time integration technique for pseudodynamic testing - Error propagation analysis*, Soil Dynamics & Earthquake Engineering, Vol. 16, Issue 7-8, pp. 427-443, 1997.

[6] R. Sajeeb, D. Roy & C.S. Manohar, *Numerical aspects of a real-time sub-structuring technique in structural dynamics*, International Journal for Numerical Methods In Engineering, Vol. 72, Issue 11, pp. 1261-1313, 2007.

[7] B. Wu, G.S. Xu, Q.Y. Wang, *Operator-splitting method for real-time substructure testing*, Earthquake Engineering and Structural Dynamics, Vol. 35, Issue 3, pp. 293-314, 2006.

[8] B. Wu, H. Bao, J. Ou, *Stability and accuracy analysis of the central difference method for real-time substructure testing*, Vol. 34, Issue 7, pp. 705-718, 2005.

[9] G. Mosqueda and M. Ahmadizadeh, *Combined Implicit or Explicit Integration Steps for Hybrid Simulation*, Earthquake Engineering and Structural Dynamics, Vol. 36, Issue 15, pp. 2325-2343, 2007.

[10] P. A. Bonnet, M. S. Williams & A. Blakeborough. *Evaluation of numerical time-integration schemes for real-time hybrid testing*, Earthquake Engineering And Structural Dynamics, vol. 37, Issue 13, pp. 1467-1490, 2008.

[11] C. Chen, J. M. Ricles, M. M. Thomas and M. Oya, *Real-time hybrid testing using the unconditionally stable explicit CR integration algorithm*, Earthquake Engineering And Structural Dynamics, Vol. 38, pp. 23-44, 2009.

[12] F. A. Lülf, T. Duch-Minh and R. Ohayon, *Reduced bases for nonlinear structural dynamic systems: A comparative study*, Journal of Sound and Vibration, Volume 332, Issue 15, pp. 3897-3921, 2013.

[13] A. Blakeborough, M. S. Williams, A. P. Darby, *The development of real-time substructure testing*, Philosophical Transactions of the Royal Society A: Mathematical, Physical and Engineering Sciences, Volume 359, Issue 1786, pp. 1869-1891, 2001.

[14] Y. Shi & C. Mei, *A finite element time domain modal formulation for large amplitude free vibrations of beams and plates*, Journal of Sound and Vibration, Volume 193, Issue 2, pp. 453-464, 1996

[15] R. D. Cook, D. S. Malkus, M. E. Plesha and R. J. Witt, *Concepts and Applications Of Finite Element Analysis*, John Wiley & Sons, fourth edition, New York, USA, 1974.

[16] S. Krenk, *Non-linear Modeling and Analysis of Solids and Structures*, Cambridge University Press, Cambridge, UK, first edition, 2009.

[17] T. Belytschko, W. K. Liu, B. Moran, *Nonlinear Finite Elements for Continua and Structures*, John Wiley & Sons, Chicester, England, first edition, 2000.

[18] A. P. Boresi et al., *Advanced Mechanics Of Materials*, John Wiley & Sons, New York, USA, sixth edition, 1993.

[19] www.fiberline.com, date: 12/15/13.